Barium vacancies as the origin of triboluminescence in hexacelsian ceramics: An *ab initio* and experimental investigation

Ekaterina Novitskaya[a,#], Mahdi Amachraa[b,#], Fabián Martínez-Pallares[b], Frank Güell[c], Virginia Gómez[d], Shyue Ping Ong[b,e,*], Manuel Herrera[f,*], Olivia A. Graeve[a,b,*]

[a] Department of Mechanical and Aerospace Engineering, University of California San Diego, La Jolla, CA 92093-0411, USA
[b] Program in Materials Science and Engineering, University of California San Diego, La Jolla, CA 92093-0418, USA
[c] ENFOCAT-IN^{2}UB, Universitat de Barcelona, Catalunya, Spain
[d] Instituto de Química, Universidad Nacional Autónoma de México, 04510 CDMX, México
[e] Department of NanoEngineering, University of California San Diego, La Jolla, CA 92093-0448, USA
[f] Centro de Nanociencias y Nanotecnología, Universidad Nacional Autónoma de México, 22800 Ensenada, México

[#] Authors contributed equally to this work
[*] Corresponding authors [OAG: ograeve@ucsd.edu, http://graeve.ucsd.edu, orcid.org/0000-0003-3599-0502; MH: zaldivar@cnyn.unam.mx, orcid.org/0000-0002-7179-654X; SPO: ongsp@ucsd.edu, orcid.org/0000-0001-5726-2587]

Keywords

Triboluminescence, cathodoluminescence, silicate, vacancy, electron paramagnetic resonance.

Abstract

We describe the triboluminescence response of undoped ($BaAl_2Si_2O_8$, *h*–BAS) and Eu-doped (*h*–BAS:Eu) barium hexacelsian powders, and show that the triboluminescence behavior is dependent on the formation of barium vacancies. X-ray photoelectron spectroscopy of the *h*–BAS:Eu powders confirms the presence of Eu^{3+} and Eu^{2+} in the compound, leading to the formation of significant vacancy point defects in excess of those found in *h*–BAS as a result of the charge imbalance caused by the substitution of Eu^{3+} in Ba^{2+} sites. From electron paramagnetic resonance measurements and density functional theory (DFT) calculations, we demonstrate that the vacancy defects correspond to singly ionized barium vacancies. DFT calculated thermodynamic transitions and electronic structure calculations reveal deep energy levels within the compound's energy band gap, with a strong emission at 3.33 eV correlated to an electron exchange between the conduction band minimum and a barium vacancy center. Time-resolved triboluminescence spectra show that the increased concentration of barium vacancies in *h*–BAS:Eu enhances the signal by about 75% compared to the signal from *h*–BAS. These results play an important role in the understanding of fundamental mechanisms behind the triboluminescence response of ceramic materials, as well as the role of different types of defects in this process.

1. Introduction

Triboluminescence is a specific type of luminescence that is produced during the propagation of a crack within a solid.[1-3] As a crack propagates through the material, visible light emission is produced at the crack tip, a phenomenon which has been investigated in several types of materials for use as stress indicators for smart sensors of structural damage,[4,5] the visualization of stress distributions,[6,7] and nondestructive testing.[8] Accordingly, there are two main subtypes of triboluminescence, namely deformation triboluminescence and electrically-, thermally- and chemically-induced triboluminescence. The phenomenon has been observed in alkali halide crystals, II–VI compounds, alkaline earth oxides, and metals.[9-12] Unfortunately, the emission intensities of these materials have proven to be low for use in practical applications.

The mechanisms of triboluminescence are still not well understood, but several models have been proposed and described in literature,[13,14] including vacancy point defects as the origin of such signals. For example, Nakayama[15] reported the generation of a broad triboluminescence signal from 400 to 700 nm for single crystal MgO, assigning its origin to F centers (oxygen vacancies containing two trapped electrons) and F^+ centers (oxygen vacancies containing one trapped electron). Miura *et al*.[16] reported a triboluminescence emission centered at about 750 nm for single crystal MgO from oxygen vacancies, and a signal at 520 nm for diamond, assigning it to nitrogen trapped at vacancy defects. More recently, Wang *et al*.[17] reported two triboluminescence signals centered at 420 and 475 nm for ZnS crystals, attributing them to F_S^+ centers (sulfur vacancies containing one trapped electron) and acceptor-type zinc vacancies, respectively. We recently reported the mechanoluminescence response of MgO powders,[18] showing a pronounced signal because of the presence of two types of oxygen vacancies, namely F and M centers.

Several researchers have found a triboluminescence response from barium hexacelsian, ($BaAl_2Si_2O_8$, *h*–BAS), doped with small amounts of rare-earth ions (*h*–BAS:RE), including samarium, ytterbium, cerium, europium,[19,20] and dysprosium,[21] where the color of the emission can be adjusted by changing the type of rare-earth ion dopant, allowing control over the signal type such that emissions ranging anywhere from the red to the blue region of the electromagnetic spectrum can be achieved. Thus, the presence of the dopant presumably has an effect by modifying the wavelength of the triboluminescence signal. However, none of these studies undertook an analysis of the triboluminescence response of an undoped BAS specimen. In addition, in some cases there was a shift in signal between the photoluminescence and triboluminescence spectra,[19] which was later shown to be an artifact of testing methodology.[20] For the case of *h*–BAS:Eu, the photoluminescence spectrum has been shown to exhibit a bright emission line at 3.33 eV (371 nm) and a weak and very broad emission centered around 2.55 eV (485 nm).[4,22,23] The triboluminescence spectrum for this material has the same emission located at around 3.30 eV (375 nm), while the broad band is centered around 2.58 eV (480 nm).[20] These signals have been attributed to the Eu^{2+} electronic transitions from the $4f^6 5d$ ground state levels, caused by the application of mechanical energy and subsequent emission upon electron relaxation.[22]

In this study, we describe the luminescence response of *h*–BAS and *h*–BAS:Eu using a combination of experimental characterization techniques and density functional theory calculations. Photoluminescence and cathodoluminescence in both *h*–BAS and *h*–BAS:Eu reveal a 3.33 eV (372 nm) emission. Computational calculations attribute this luminescence to stable defect centers leading to impurity levels, other than those of europium, within the $BaAl_2Si_2O_8$ energy band gap. X-ray photoelectron spectroscopy reveals a significant presence of Eu^{3+} and

electron paramagnetic resonance the presence of barium vacancies. Combining electron paramagnetic resonance with computed transition energies, we confirm the presence of singly-ionized barium vacancies of negative charge (v'_{Ba}) as the luminescence center of the observed 3.33 eV emission in both *h*-BAS and *h*–BAS:Eu. Increased triboluminescence intensity in *h*–BAS:Eu compared to the undoped *h*–BAS is caused by the higher concentration of the barium vacancy luminescence centers.

2. Experimental and Computational Procedures

A. Experimental Procedures

$BaAl_2Si_2O_8$ powders were synthesized by solution combustion synthesis (SCS)[24] using nitrates of barium and aluminum as oxidizers, amorphous fumed silica as a source of silicon, and carbohydrazide as organic fuel.[25-31] The reagents used were barium nitrate [$Ba(NO_3)_2$, 99+%, Alfa Aesar, Ward Hill, MA], aluminum nitrate hydrate [$Al(NO_3)_3$•$9H_2O$, 98-102%, Alfa Aesar, Ward Hill, MA], amorphous fumed silica [SiO_2, S.A. 350-420 m^2/g, 325 mesh powder, Alfa Aesar, Ward Hill, MA], and carbohydrazide [$CO(NHNH_2)_2$ 97%, Alfa Aesar, Ward Hill, MA]. A mixture of 3.30 g of $Ba(NO_3)_2$, 9.97 g of $Al(NO_3)_3$•$9H_2O$, 1.60 g of SiO_2, and 10.78 g of $CO(NHNH_2)_2$ were dissolved in 100 mL of deionized water. The solution was stirred for 30 minutes. Next, the solution was placed in a muffle furnace at 773 K. After water evaporation, the mixture combusted and the resulting powders were gathered for thermal treatment at 1473 K for 2 hours. These powders will be referred to as *h*–BAS. In addition, a europium-doped *h*–BAS:Eu powder was obtained by additionally adding 0.30 g of $Eu(NO_3)_3$•$6H_2O$ [Alfa Aesar, Ward Hill, MA] to the precursor mixture and following the methodology described above.

The morphology of the powders was analyzed by scanning electron microscopy (FEI-XL30, FEI Company, Hillsboro, OR) using 10 kV accelerating voltage. For imaging, all samples were mounted on aluminum sample holders and sputter-coated with iridium. Phase and crystallite size of the powders were characterized by X-ray diffraction on a D2 Phaser (Bruker AXS, Madison, WI) using a step size of 0.02 degrees 2θ and a count time of 1 s, scanning from 15 to 85 degrees 2θ. Crystallite sizes of the powders were calculated using TOPAS 4.2 software (DIFFRAC Topas, Bruker AXS, Madison, WI) by means of Rietveld refinement. Particle sizes for all the powders were analyzed by dynamic light scattering[32-37] a Nanotrac ULTRA (Microtrac Inc., York, PA, USA) system by dispersing approximately 25 mg of powders in 25 mL of ethanol, stirring for 15 minutes, and ultrasonicating for 15 minutes. X-ray photoelectron spectroscopy measurements were obtained on a SPECS (Berlin, Germany) system equipped with a PHOIBOS 150 WAL analyzer with DDL-2 detector, and a FOCUS 500/600 ellipsoidal monochromatic X-ray source with a dual anode of Al and Ag. High-resolution spectra were obtained using 300 scans during the measurement with windows of 0.1 eV sensitivity. To estimate the areal intensity of Eu^{3+} and Eu^{2+} components, we deconvoluted final spectra into Gaussian peaks using a Shirley background with the aid of CasaXPS processing software.

The photoluminescence excitation and emission spectra were obtained on a Hitachi F-4500 (Tokyo, Japan) fluorescence spectrophotometer equipped with a Xe lamp (150 W) as excitation source. The emission spectra were acquired by exciting the sample using a 305 nm excitation wavelength. Cathodoluminescence measurements were performed on a scanning electron microscope using a Gatan MonoCL4 system at 300 K in the UV-visible spectral range.[38,39] Cathodoluminescence time-resolved curves were obtained by measuring changes in the monochromatic cathodoluminescence intensity as a function of the time during electron beam

irradiation of samples, obtained by operating the scanning electron microscope at 15 keV with a beam current of 1 nA. An approximate surface area of 3060 μm^2 was irradiated resulting in a beam current density of 3.2×10^{-13} A/μm^2. Triboluminescence spectra were obtained using a drop tower testing methodology. The instrument built for this purpose consisted of a polyvinyl chloride (PVC) pipe of 1.5 cm inner diameter, drilled on the upper side with a hold for a pin that supported a 1.27 cm diameter steel ball (13.8 g). Upon removal of the pin, the steel ball dropped from a height of 0.905 m and impacted the sample placed on a steel plate at the bottom of the PVC pipe. The resulting luminescence signal was recorded by using a fused silica optical fiber attached to a Hamamatsu R928 photomultiplier tube. The detected panchromatic signal was amplified with a Keithley 2400 current amplifier converting the current signal to a voltage signal and finally capturing with a Hantek DSO5102P oscilloscope. Ten spectra were independently recorded for each sample and averaged. The paramagnetic species present in the powders were identified using the electron paramagnetic resonance technique using a JEOL JES-TE300 system (Tokyo, Japan), acquiring spectra with an absorption frequency of 9.4 GHz at ambient (298 K) temperature, and a microwave power of 10 mW. The resulting spectra were simulated and fitted using the EasySpin open-source MATLAB software package.[40]

B. Computational Procedures

All DFT calculations were performed using the Vienna *ab initio* simulation package (VASP) within the projected-augmented wave method.[41,42] Structural optimization of *h*–BAS was computed using the general gradient approximation Perdew-Burke-Ernzerhof (PBE) functional, with a plane wave energy cutoff of 520 eV. The Brillouin zone was integrated using a *k*-point grid density of at least 100 $Å^{-3}$. ~~For calculations on Eu^{2+}-activated *h*–BAS (*h*–BAS:Eu^{2+}), we used the PBE+*U* method with an effective *U* value of 2.5 eV for the highly localized 4*f*~~

~~electrons of Eu^{2+}. The energies and forces were converged up to 10^{-5} eV and 0.01 eV•$Å^{-1}$, respectively, with a *k*-point density of at least 15 $Å^{-1}$. A 3×3×2 supercell of the *h*–BAS with at least 10 Å on each lattice parameter (with an effective Eu^{2+} concentration of 5%) was used for the *h*–BAS:Eu^{2+} calculations.~~

In general, the formation energy (E^f) of a defect X of charge q is a function of the electron Fermi energy (E_F) and the atomic chemical potential (μ_i) and is expressed as follows:

$$E^f\left[X^q\right] = E_{tot}\left[X^q\right] - E_{tot}\left[\text{pristine}\right] - \sum_i n_i\mu_i + qE_F + q\Delta V \quad (1)$$

where, $E_{tot}[X^q]$ is the total energy of the supercell lattice with defect X of charge q, E_{tot}[pristine] is the total energy of the pristine system, n_i indicates the number of species i being removed ($n_i < 0$) or added ($n_i > 0$) from the supercell, and ΔV is the potential alignment correction term accounting for the spurious electrostatic interactions between charged supercells and for the finite *k*-point sampling at the Γ zone center. To correct the artificially repeated charge between supercells in the total energy and in the one-electron eigenvalues and eigenstates, we utilized the self-consistent potential correction method for charge periodic systems where a corrective potential ΔV is included in the Kohn-Sham equations.[43] The atomic chemical potential can be further decomposed as $\mu_i = E_i + \Delta\mu_i$, where $\Delta\mu_i$ is the restricted chemical potential range referenced to the elemental solid or gas with energy E_i. Equation (1) can therefore be rearranged as follows:

$$E^f\left[X^q\right] = E_0^f\left[X^q\right] - \sum_i n_i\Delta\mu_i + qE_F + q\Delta V \quad (2)$$

$$E_0^f\left[X^q\right] = E_{tot}\left[X^q\right] - E_{tot}\left[\text{pristine}\right] - \sum_i n_i E_i \quad (3)$$

The constrained range of $\Delta\mu_i$ is typically set such that the formation of all single elements is circumvented, the decomposed products in equilibrium with the defect phase are not allowed to form, and the thermodynamic stability of the pristine structure is maintained.[44]

3. Results and Discussions

Figure 1 illustrates the X-ray diffraction (XRD) pattern of the *h*–BAS (Figure 1a) and *h*–BAS:Eu (Figure 1b) powders corresponding to the hexacelsian phase of $BaAl_2Si_2O_8$ (PDF# 01-072-7502). A small impurity of $BaAl_2O_4$ (PDF# 00-017-0306) was identified in both patterns. Similar results were previously reported for hexacelsian powders produced by combustion synthesis.[22] All indexed peaks in *h*–BAS:Eu correspond to those of the undoped *h*–BAS phase, confirming that no secondary phases of europium oxide were formed during powder synthesis. The crystallite sizes from XRD are 138 ± 2 nm and 105 ±1 nm and the particle sizes from dynamic light scattering are 408 ± 47 nm and 491 ± 146 nm for the *h*–BAS and *h*–BAS:Eu powders, respectively. Thus, no significant differences between the crystallite and particle sizes of the undoped and doped powders were identified. Specifically, the particle sizes were found to be between roughly 300 and 600 nm, which is in agreement with Sinha *et al*.[22] who reported an average *h*–BAS:Eu particle size of 420 nm. Scanning electron microscopy reveals a porous powder morphology (Figure 2) typical of combustion-synthesized powders.[45]

The photoluminescence emission spectra of both *h*–BAS and *h*–BAS:Eu (Figure 3a-b) show a strong emission centered at 3.33 eV (372 nm). The excitation spectrum of the *h*–BAS powder (Figure 3a), obtained by measuring the intensity of the 3.33 eV emission, exhibits a dominant band centered at 4.05 eV (306 nm) and a shoulder at 3.83 eV (324 nm), as well as a weak band at about 4.76 eV (260 nm). The excitation spectrum of the *h*–BAS:Eu powder (Figure

3b) exhibits the same absorption bands, although there is an evident increase in the relative intensity of the 3.83 eV emission compared to the 4.05 eV emission. Thus, both compounds are intrinsically similar in their photoluminescence behavior, meaning that the response is a consequence of an intrinsic defect present in both materials, and not connected to the presence of europium dopant.

X-ray photoelectron spectroscopy in Figure 4 reveals the presence of 0.27 at.% Eu^{3+} (1135 eV) and 0.03 at.% Eu^{2+} (1124 eV) in our *h*–BAS:Eu powder, a ratio of 9:1 of Eu^{3+} with respect to Eu^{2+}. Because of the charge imbalance caused by substitution of Eu^{3+} into the Ba^{2+} sites of the *h*–BAS lattice, the formation of interstitial oxygen defects and/or the formation of barium vacancies is necessary for charge compensation. The theoretical defect reaction describing the formation of barium vacancies can be represented by:

$$3\ Ba_{Ba}^{\times} \xrightarrow{2\left[Eu^{3+}\right]} 2\left[Eu^{3+}\right]_{Ba}^{\bullet} + v_{Ba}'' \qquad (4)$$

where ×, •, and ’ refer to neutral, positive, and negatively charged point defects, and v refers to a vacancy site. From density functional theory (DFT) calculations, we find that the formation of barium vacancies has the lowest E^f of 4.77 eV/defect (the lower bound of the chemical potential is $\Sigma n_i \Delta\mu_i$ = 1.19 eV), while the formation of interstitial oxygen has a significantly higher E^f of 5.90 eV/defect ($\Sigma n_i \Delta\mu_i$ = 0.65 eV). It is therefore likely that the stabilization of Eu^{3+} in the *h*–BAS lattice is accompanied by the formation of barium vacancies.

Experimentally, the electron paramagnetic resonance (EPR) technique was employed to identify the presence of paramagnetic radicals associated with barium vacancies and Eu^{2+} ions, since the presence of charged point defects could potentially lead to charge-state thermodynamic transition levels and consequently optical transitions within both *h*–BAS and *h*–BAS:Eu. Figure

5a illustrates the experimental EPR spectrum obtained for the *h*–BAS powder and Figure 5b the corresponding simulated curve using a *g* value of 1.974. This gyromagnetic value matches well with a previously reported *g* value of single ionized barium vacancies (v'_{Ba}) in $BaTiO_3$ ceramics[46-48] and in $BaSnO_3$ nanostructures.[49] Furthermore, Kutty *et al.*[50] reported an EPR signal with a *g* value of 1.997 attributed to v'_{Ba} defects present in the orthorhombic and rhombohedral phases of $BaTiO_3$, observing that the value remains unchanged with variations in the spatial distribution of the electric field present in these two different crystalline lattices. Accordingly, our measured *g* value confirms the presence of v'_{Ba} defects in *h*–BAS. Furthermore, Figure 5c shows the experimental and simulated EPR spectra for the *h*–BAS:Eu powder. The components of the simulated EPR spectra corresponding to the v'_{Ba} signal ($g = 1.974$), and the EPR multiplets generated by the interaction between the seven unpaired electrons in the 4*f* orbitals of Eu^{2+}, were calculated with an axial zero-field splitting (ZFS) parameter *D* of 990 MHz using the EasySpin MATLAB toolbox. The Eu^{2+} ion has a $4f^7$ electronic configuration and therefore an $S = 7/2$ ground state (orbital angular momentum, $L = 0$), whereas Eu^{3+} ions have a non-magnetic $^7F_0$ single ground state with an $S = 0$ because the spins of the six unpaired electrons are paired in opposite directions, thus not contributing to the EPR signal. For EPR multiplets, we assumed an origin to the spin-orbit coupling between the Eu^{2+} unpaired electrons and the splitting by crystal field effects along the different axial directions in the BAS crystal, both evaluated by the axial ZFS parameter *D*. Some authors have reported Eu^{2+} EPR multiplets in BAS powders.[51,52] However, there are no specific reports on ZFS calculations to identify the presence of the v'_{Ba} EPR signal. Additionally, Figure 5 shows that the intensity of the v'_{Ba} signal in *h*–BAS:Eu

exhibits higher intensity compared to the signal from *h*–BAS, revealing an increase in the density of v'_{Ba} defects.

The cathodoluminescence technique was also used to identify the optically active centers in the *h*–BAS and *h*–BAS:Eu powders. In this technique, the electron beam excitation may produce significantly greater carrier generation rates compared to typical optical excitations from photoluminescence. In general, this leads to emissions from all the luminescence transitions present in the material.[53,54] Figure 6a illustrates the cathodoluminescence spectrum obtained from the undoped *h*–BAS powder, revealing a peak centered at 2.06 eV (602 nm) and a broad peak centered at about 3.82 eV (325 nm) with shoulders at 2.90 eV (428 nm) and 3.33 eV (372 nm). Figure 6a also shows a deconvolution of the spectrum to obtain the individual transitions, calculated using Gaussian curves with a FWHM of 0.5 eV and centered at 2.06 eV (602 nm), 2.85 eV (435 nm), 3.33 eV (372 nm), 3.80 eV (326 nm), and 4.21 eV (295 nm). We fixed the FWHM to a value of 0.5 eV for each component because this parameter represents the inhomogeneous broadening of the linewidths generated by crystallinity disorder associated with vacancies and other point defects in the samples.[55] The coefficient of determination R^2 for such deconvolution was 0.9870. The component centered at 3.33 eV likely corresponds to the photoluminescence emission shown in Figure 3. Thus, it is seen that both photoluminescence and cathodoluminescence measurements display the presence of the 3.33 eV emission.

Furthermore, the cathodoluminescence spectrum of the *h*–BAS:Eu powder reveals a very significant emission enhancement at 3.33 eV (Figure 6b), which can be attributed to the increased concentration of barium vacancies. Additionally, this spectrum also reveals two weak signals at ~2.0 eV (620 nm) and ~2.1 eV (590 nm) (see inset in Figure 6b), corresponding to the transitions $^5D_0$–$^7F_2$ and $^5D_0$–$^7F_0$, respectively, for the Eu^{3+} ions[38] that were detected as the

majority europium ions in X-ray photoelectron spectroscopy (see Figure 4). Thus, Eu^{3+} is not only the supplier of traps, from the charge imbalance caused by the substitution of Eu^{3+} into Ba^{2+} sites, but also a minor luminescence activator. Based on the significant difference in peak intensities between the signal at 3.33 eV and the Eu^{3+} signal at ~2.0 eV, it is clear that the luminescence in this material is controlled by the presence of vacancies. Thus, the Eu^{3+} is important as a producer of traps, and not as the source of luminescence emission by itself. The absence of several peaks (2.06, 2.85, 3.82, and 4.24 eV) in the cathodoluminescence spectra of the *h*–BAS:Eu powder is due to the higher concentrations of barium vacancies that produce a very strong emission at 3.33 eV and that result in the other signals appearing as noise and buried within the spectrum at very low intensities (Figure 6b).

To understand the effect of barium and oxygen vacancies in the luminescence process, we used self-consistent DFT calculations to investigate the stability of charged point defect states (X^q) in *h*–BAS. Figure 7a describes the response of $E^f[X^q]$ with respect to the Fermi energy (E_F). Between the top of the valence band (at a Fermi energy of 0 eV) and the bottom of the conduction band (at a Fermi energy of 4.92 eV), we find three deep energy states. One is associated with oxygen vacancies (blue line) at 0.85 eV. The other two are associated with barium vacancies (red line) at 0.88 and 2.34 eV. Here, the energy required to remove or add electrons from the valence and conduction bands is much larger than the thermal energy k_BT. We computed the thermodynamic transition energies, $\varepsilon(q/q')$, as follows:

$$\varepsilon\left(q/q'\right)=\frac{E^{\mathrm{f}}\left[X^{q};\,E_{\mathrm{F}}=0\right]-E^{\mathrm{f}}\left[X^{q'};\,E_{\mathrm{F}}=0\right]}{q'-q} \tag{5}$$

where $E^{\mathrm{f}}\left[X^{q};\,E_{\mathrm{F}}=0\right]$ is the formation energy of a defect X of charge q when E_F is defined at the valence band maximum (VBM), as shown in Figure 7b. Barium vacancies present three different

charged states within the band gap, -2, -1, and 0 (see Figure 7a), leading to two charge transition levels, namely ε(0/-1) and ε(-1/-2). For oxygen vacancy defects, a single transition level of ε(1/0) is located above the VBM, while the ε(2/1) level is located 0.83 eV below the VBM. The zero-phonon line (ZPL) energy, which defines the energy difference between an excited state and a ground state, is now used to elucidate the origin of the observed optical transitions from photoluminescence and cathodoluminescence. Upon light excitation, an electron could be lifted from a neutral oxygen vacancy ($v_O^{\times}$), resulting in a positively charged vacancy and a free electron, described by:

$$v_O^{\times} + \hbar\omega \longrightarrow v_O^{\bullet} + e' \tag{6}$$

For the case of a singly ionized (v'_{Ba}) barium vacancy, excitation could result in a neutral barium vacancy and a free electron, described by:

$$v'_{Ba} + \hbar\omega \longrightarrow v_{Ba}^{\times} + e' \tag{7}$$

This may lead to radiative transitions due to the recombination of a conduction band electron and a hole in the $v_O^{\bullet}$ or $v_{Ba}^{\times}$ gap states. The computed ZPL energies of equations (6) and (7) are 4.07 eV and 4.04 eV for $v_O^{\times}$ and v'_{Ba}, respectively (see Figure 7b). Moreover, the Coulomb attraction in equation (4) is the strongest as it occurs between a negatively charged electron and two positively charged holes from the neutral barium vacancy. Consequently, the radiative transition described by equation (7) with ZPL energy of 4.04 eV is assigned to the observed 4.05 eV absorption peak in Figure 3a-b.

For the 4.05 eV absorption peak (see Figure 3b), the electronic excitation is depicted in Figure 8a as an electronic transition between the energy level calculated for the v'_{Ba} at the ZPL

energy and the conduction band. In this transition, the barium vacancies adopt a neutral charge ($v_{Ba}^{\times}$) modifying the spatial charge of its neighbor atoms and rearranging them as a lattice relaxation. Figure 8b shows a schematic configurational coordinate diagram for a $v_{Ba}^{\times}$ defect representing the electronic transition from the conduction band to a vibronic state generated by the strong Coulombic attraction between a negative electron and a neutral barium vacancy [equation (7)], which we propose is responsible for the strong 3.33 eV emission seen in Figures 3 and 6. In considering Figure 6a, we see that there are dominant emission peaks at 3.33 and 3.80 eV. The 3.33 eV emission is now clear with respect to its provenance. Regarding the emission at 3.80 eV, we propose that it could originate from the attraction between a negative electron and a positively charged oxygen vacancy ($v_{O}^{\bullet}$), shown in Figure 8a as a 4.07 eV absorption and in Figure 8b as the subsequent 3.80 eV emission.

Figure 9 illustrates the cathodoluminescence intensity variation of the 3.33 eV emission with the electron beam exposure time observed for the *h*–BAS and *h*–BAS:Eu powders under irradiation with a voltage of 15 keV and beam current of 1 nA. The curves obtained reveal an exponential function with values for the coefficient of determination R^2 of 0.8927 for *h*–BAS and 0.7372 for *h*–BAS:Eu. The saturation intensities for the *h*–BAS and *h*–BAS:Eu powders were 3.22 and 108 kcps, respectively, occurring at times of about 80 and 20 s, thus the undoped powders exhibit a saturation time that is around four times higher compared to the doped powders. Knowing that the 3.33 eV emission corresponds to the electronic transition between barium vacancy states, we propose that electron beam irradiation generates some of these vacancies, increasing their concentration, n_v, up to a thermodynamic limit (*i.e.*, saturation) described by a thermally activated process that follows the Arrhenius behavior:

$$n_v = n_o \exp\left(-\frac{E_F}{k_B T}\right) \quad (8)$$

where n_o is the saturation concentration of vacancies, E_F is the vacancy formation energy, and k_B is Boltzmann's constant.

To confirm that electron beam irradiation induces the necessary energy in *h*–BAS to produce barium vacancies, we used Monte Carlo simulations to evaluate the energy per atom absorbed from an electron beam with a current of 1 nA and energy of 15 keV. We simulated the energy loss of 1×10^6 incident electrons on the surface of a solid with the atomic composition and density of *h*–BAS, using the Casino v2.51 software, selecting a Mott cross-section and Joy and Luo[56] empirical equations to evaluate the energy loss of electrons after stochastically scattering processes. This simulation revealed that at a depth of ~410 nm from the *h*–BAS surface, the incident electrons contain 50% of their initial energy of 15 keV due to scattering by the solid, representing the average between electron penetration depth and percent of energy transferred to the solid. Thus, considering that the irradiated area for the curves shown in Figure 9 was 62.5 μm × 62.5 μm at a scanning frequency of 0.25 sec^{-1}, the irradiated volume for a depth of 410 nm corresponds to 400 $\mu m^3 \cdot sec^{-1}$. Furthermore, from the *h*–BAS atomic density of 5.30×10^9 $atoms \cdot \mu m^{-3}$, calculated from the *h*–BAS density of 3.305 $g \cdot cm^{-3}$ and molecular weight of 375.45 $g \cdot mol^{-1}$, we obtained that the number of irradiated atoms per second at a depth of ~410 nm is 2.12×10^{12} sec^{-1}. Additionally, from the electron beam energy and current of 15 keV and 1 nA, respectively, the total electron energy per second is 1.5×10^5 $J \cdot s^{-1}$ or 9.36×10^{13} $eV \cdot s^{-1}$ (50% of this energy is 4.68×10^{13} $eV \cdot s^{-1}$ absorbed at 410 nm from the *h*–BAS surface). Finally, we calculated the absorbed energy per atom by dividing 4.68×10^{13} $eV \cdot s^{-1}$ by the number of irradiated atoms per second (2.12×10^{12} sec^{-1}), obtaining a value of 22.1 eV, which is

significantly higher than the formation energy of barium vacancies of around 11 eV (Figure 7a), confirming our assumption that electron beam irradiation generates barium vacancies in *h*–BAS following a thermal activation mechanism. Table 1 lists the calculated absorbed energies per atom for different penetration depths of the electron beam, listing energy values higher than 11 eV for depths between 300 and 1000 nm, thus confirming the viability of forming barium vacancies. Based on these considerations, we propose that the *h*–BAS powders exhibit a longer saturation time to reach the maximum intensity of the 3.33 eV emission because these powders do not contain significant barium vacancies, as we see in *h*–BAS:Eu. The electron beam induces the formation of the vacancies and the cathodoluminescence intensity reaches a maximum once the vacancies reach a stable concentration.

Figure 10 illustrates the triboluminescence 3.33 eV signal obtained for the *h*–BAS (Figure 10a) and *h*–BAS:Eu (Figure 10c) powders, revealing maximum intensities of about 80 and 140 V, respectively. This difference demonstrates the enhancement of triboluminescence response for *h*–BAS:Eu of roughly 75% compared to *h*–BAS. We propose that the triboluminescence signal is generated by barium vacancies acting as luminescence centers, which are present in the *h*–BAS:Eu powder at higher concentrations compared to the *h*–BAS powder. A fitting for the triboluminescence decay signal for both *h*–BAS (Figure 10c) and *h*–BAS:Eu (Figure 10d) describe an exponential decay following:

$$I_{TL} = A \exp\left\{-\frac{t}{\tau}\right\} \tag{9}$$

where I_{TL} is the triboluminescence intensity, t is time, and τ is the decay time. These results reveal that both *h*–BAS and *h*–BAS:Eu exhibit very similar decay time values of 5×10^{-5} and 4×10^{-5} seconds, respectively, showing that the triboluminescence signal from both samples has the

same origin, namely the electronic transitions between energy levels generated by the presence of barium vacancies acting as luminescence centers.

In summary, the nature of the triboluminescence response of *h*–BAS and *h*–BAS:Eu materials was identified. The existence of large concentrations of barium vacancies in *h*–BAS:Eu, produced by the incorporation of Eu^{3+} ions into the BAS structure, was found to be responsible for its more pronounced triboluminescence response compared to *h*–BAS. An important correlation between the existence of a 3.33 eV band in the photoluminescence and cathodoluminescence spectra of *h*–BAS:Eu and barium vacancies was also identified. The origin of the triboluminescence signal was found to be similar for both *h*–BAS and *h*–BAS:Eu, attributed to the electronic transitions between energy levels generated by the presence of barium vacancies acting as luminescence centers.

4. Conclusions

Undoped (*h*–BAS) and europium-doped (*h*–BAS:Eu) $BaAl_2Si_2O_8$ powders were synthesized by solution combustion synthesis, resulting in particles with diameters between 300 and 600 nm. The incorporation of Eu^{3+} and Eu^{2+} ions in the *h*–BAS:Eu powders was verified by X-ray photoelectron spectroscopy, with the dopant not affecting the crystal structure or resulting in the formation of any secondary phases. Photoluminescence emission spectra for both the undoped and doped powders demonstrated a strong emission centered at 3.33 eV, while the photoluminescence excitation spectra revealed two bands centered at 3.83 eV (324 nm) and 4.05 eV (306 nm). Cathodoluminescence characterization also confirmed the presence of a 3.33 eV emission for both samples, with a considerably higher intensity in the *h*–BAS:Eu powder.

Self-consistent DFT calculations confirmed that the presence of the 3.33 eV band is due to the existence of barium vacancies. The presence of these vacancies was also verified from cathodoluminescence spectra, which demonstrated a pronounced difference in the cathodoluminescence saturation time between the *h*-BAS and *h*-BAS:Eu powders. Electron paramagnetic resonance (EPR) measurements confirmed the single negative charge of the barium vacancies (v'_{Ba}). In addition, EPR spectral deconvolution of the *h*–BAS:Eu spectrum revealed resonances associated with the presence of Eu^{2+} ions in addition to the v'_{Ba} . Triboluminescence measurements showed an emission signal in both powders, attributed to the electronic transitions between energy levels generated by the presence of the v_{Ba} acting as luminescence centers. The response shows an enhancement of 75% in the *h*–BAS:Eu compared to *h*–BAS powders. These results play an important role in the understanding of fundamental mechanisms behind the triboluminescent response of ceramic materials, as well as the role of different types of defects in this process. These insights show a path for the potential use of these materials in structural health monitoring applications.

Acknowledgements

This work was supported by a grant from the National Science Foundation (No. 1911372), and grants from CONACyT (No. 284667) and UCMEXUS (No. CN-19-137). The computational resources necessary for this work were provided by the Extreme Science and Engineering Discovery Environment (XSEDE) supported by the National Science Foundation, the Triton Supercomputer Center (TSCC) at the University of California San Diego, and the National Energy Research Scientific Computing Center (NERSC).

DATA AVAILABILITY STATEMENT

The data that support the findings of this study are available from the corresponding authors upon reasonable request.

References

(1) Chandra, B. P. Squeezing light out of crystals: Triboluminescence. *Nucl. Tracks Radiat. Meas.* **1985**, *10* (1-2), 225–241. DOI: 10.1016/0735-245X(85)90028-6.

(2) Zink, J. I. Triboluminescence. *Acc. Chem. Res.* **1978**, *11* (8), 289–295. DOI: 10.1021/ar50128a001.

(3) Sage, I.; Bourhill, G. Triboluminescent materials for structural damage monitoring. *J. Mater. Chem*. **2001**, *11* (2), 231–245. DOI: 10.1039/B007029G.

(4) Sage, I.; Badcock, R.; Humberstone, L.; Geddes, N.; Kemp, M.; Bourhill, G. Triboluminescent damage sensors. *Smart Mater. Struct.* **1999**, *8* (4), 504–510. DOI: 10.1088/0964-1726/8/4/308.

(5) Olawale, D. O.; Dickens, T.; Sullivan, W. G.; Okoli, O. I.; Sobanjo, J. O.; Wang, B. Progress in triboluminescence-based smart optical sensor system. *J. Lumin*. **2011**, *131* (7) 1407–1418. DOI: 10.1016/j.jlumin.2011.03.015.

(6) Xu, C. -N.; Zheng, X. -G.; Akiyama, M.; Nonaka, K.; Watanabe, T. Dynamic visualization of stress distribution by mechanoluminescence image. *Appl. Phys. Lett*. **2000**, *76*, 179–181. DOI: 10.1063/1.125695.

(7) Sohn, K. -S.; Seo, S. Y.; Kwon, Y. N.; Park, H. D. Direct observation of crack tip stress field using the mechanoluminescence of $SrAl_2O_4$:(Eu,Dy,Nd). *J. Am. Ceram. Soc*. **2002**, *85* (3), 712–714. DOI: 10.1111/j.1151-2916.2002.tb00158.x.

(8) Chandra. B. P. Acoustic and photon emissions during mechanical deformation of coloured alkali halide crystals. *J. Phys. D: Appl. Phys*. **1984**, *17* (1), 117−123. DOI: 10.1088/0022-3727/17/1/016.

(9) Metz, F.I.; Schweiger, R. N.; Leidler, H. R.; Girifalco, L. A. Stress activated luminescence in X-irradiated alkali halide crystals. *J. Phys. Chem*. **1957**, *61* (1), 86−89. DOI: 10.1021/j150547a016.

(10) Osip'yan, Yu. A.; Petrenko, V. F.; Zaretskii, A. V.; Whitworth, R. W. Properties of II–VI semiconductors associated with moving dislocations. *Adv. Phys.* **1986**, *35* (2), 115−188. DOI: 10.1080/00018738600101871.

(11) Williams Jr., G. P.; Turner, T. J. Triboluminescence in single crystal alkaline earth oxides. *Solid State Commun.* **1979**, *29* (3), 201−203. DOI: 10.1016/0038-1098(79)91038-X.

(12) Abramova, K. B.; Shcherbakov, I. P.; Rusakov, A. I.; Semenov, A. A. Emission processes accompanying deformation and fracture of metals. *Phys. Solid State* **1999**, *41* (5), 761−762. DOI: 10.1134/1.1130865.

(13) Jha, P.; Chandra, B. P. Survey of the literature on mechanoluminescence from 1605 to 2013. *Luminescence* **2014**, *29* (8), 977−993. DOI: 10.1002/bio.2647.

(14) Chandra, B. P.; Rathore, A. S. Classification of mechanoluminescence. *Cryst. Res. Technol.* **1995**, *30* (7), 885−896. DOI: 10.1002/crat.2170300702.

(15) Nakayama, K. Triboplasma generation and triboluminescence: Influence of stationary sliding partner. *Tribol. Lett.* **2010**, *37*, 215−228. DOI: 10.1007/s11249-009-9516-5.

(16) Miura, T.; Hosobuchi, E.; Arakawa, I. Spectroscopic studies of triboluminescence from a sliding contact between diamond, SiO_2, MgO, NaCl, and Al_2O_3 (0001). *Vacuum* **2009**, *84* (5), 573–577. DOI: 10.1016/j.vacuum.2009.06.035.

(17) Wang, K.; Xub, X.; Ma, L.; Wang, A.; Wang, R.; Luo, J.; Wen, S. Studies on triboluminescence emission characteristics of various kinds of bulk ZnS crystals. *J. Lumin.* **2017**, *186*, 307–311. DOI: 10.1016/j.jlumin.2017.02.006.

(18) Novitskaya, E.; Manheim, A.; Herrera, M.; Graeve, O. A. Effect of oxygen vacancies on the mechanoluminescence response of magnesium oxide. *J. Phys. Chem. C* **2021**, *125* (1), 854–864. DOI: 10.1021/acs.jpcc.0c07674.

(19) Ishihara, T.; Tanaka, K.; Fujita, K.; Hirao, K.; Soga, N. Full color triboluminescence of rare-earth-doped hexacelsian ($BaAl_2Si_2O_8$). *Solid State Commun*. **1998**, *107* (12), 763–767. DOI: 10.1016/S0038-1098(98)00271-3.

(20) Duignan, J. P.; Oswald, I. D. H.; Sage, I. C.; Sweeting, L. M.; Tanaka, K.; Ishihara, T.; Hirao, K.; Bourhill, G. Do triboluminescence spectra really show a spectral shift relative to photoluminescence spectra?. *J. Lumin*. **2002**, *97* (2), 115–126. DOI: 10.1016/S0022-2313(01)00412-4.

(21) Sahu, I. P. Luminescence properties of dysprosium doped barium alumino-silicate phosphors prepared by the solid state reaction method. *J. Mater. Sci.: Mater. Electron.* **2016**, *27* (12), 13134–13147. DOI: 10.1007/s10854-016-5459-4.

(22) Sinha, K.; Pearson, B.; Casolco, S. R.; Garay, J. E.; Graeve, O. A. Synthesis and consolidation of $BaAl_2Si_2O_8$:Eu. Development of an integrated process for luminescent smart ceramic materials. *J. Am. Ceram. Soc*. **2009**, *92* (11), 2504–2511. DOI: 10.1111/j.1551-2916.2009.03242.x.

(23) Ishihara, T.; Tanaka, K.; Hirao, K.; Soga, N. Fracto-luminescence of rare earth element-doped hexacelsian ($BaAl_2Si_2O_8$). *Jpn. J. Appl. Phys.* **1997**, *36* (Pt. 2, 6B), L781–L783. DOI: 10.1143/JJAP.36.L781.

(24) Lopez, O. A.; McKittrick, J.; Shea, L.E. Fluorescence properties of polycrystalline Tm^{3+}-activated $Y_3Al_5O_{12}$ and Tm^{3+}-Li^+ co-activated $Y_3Al_5O_{12}$ in the visible and near IR ranges. *J. Lumin*. **1997**, *71* (1), 1–11. DOI: 10.1016/S0022-2313(96)00123-8.

(25) Higgins, B.; Graeve, O. A.; Edwards, D. D. New methods for preparing submicrometer powders of the tungstate-ion conductor $Sc_2(WO_4)_3$ and its Al and In analogs. *J. Am. Ceram. Soc*. **2013**, *96* (8), 2402–2410. DOI: 10.1111/jace.12416.

(26) Kanakala, R.; Escudero, R.; Rojas-George, G.; Ramisetty, M.; Graeve, O. A. Mechanisms of combustion synthesis and magnetic response of high-surface area hexaboride compounds. *ACS Appl. Mater. Interfaces* **2011**, *3* (4), 1093–1100. DOI: 10.1021/am1012276.

(27) Kanakala, R.; Rojas-George, G.; Graeve, O. A. Unique preparation of hexaboride nanocubes: A first example of boride formation by combustion synthesis. *J. Am. Ceram. Soc*. **2010**, *93* (10), 3136–3141. DOI: 10.1111/j.1551-2916.2010.03853.x.

(28) Graeve, O. A.; Kanakala, R.; Madadi, A.; Williams, B. C.; Glass, K. C. Luminescence variations in hydroxyapatites doped with Eu^{2+} and Eu^{3+} ions. *Biomaterials* **2010**, *31* (15), 4259–4267. DOI: 10.1016/j.biomaterials.2010.02.009.

(29) Graeve, O. A.; Varma, S.; Rojas-George, G.; Brown, D. R.; Lopez, E. A. Synthesis and characterization of luminescent yttrium oxide doped with Tm and Yb. *J. Am. Ceram. Soc*. **2006**, *89* (3), 926–931. DOI: 10.1111/j.1551-2916.2006.00845.x.

(30) Shea, L. E.; McKittrick, J.; Lopez, O. A.; Sluzky, E.; Phillips, M. L. F. Advantages of self-propagating combustion reactions for synthesis of oxide phosphors. *J. Soc. Inf. Disp.* **1997**, *5* (2), 117–125. DOI: 10.1889/1.1985140.

(31) Shea, L. E.; McKittrick, J.; Lopez, O. A.; Sluzky, E. Synthesis of red-emitting, small particle size luminescent oxides using an optimized combustion process. *J. Am. Ceram. Soc*. **1996**, *79* (12), 3257–3265. DOI: 10.1111/j.1151-2916.1996.tb08103.x.

(32) Saterlie, M.; Sahin, H.; Kavlicoglu, B.; Liu, L.; Graeve, O. A. Particle size effects in the thermal conductivity enhancement of copper-based nanofluids. *Nanoscale Res. Lett*. **2011**, *6* (1), 217. DOI: 10.1186/1556-276X-6-217.

(33) Saterlie, M. S.; Sahin, H.; Kavlicoglu, B.; Liu, Y.; Graeve, O. A. Surfactant effects on dispersion characteristics of copper-based nanofluids: A dynamic light scattering study. *Chem. Mater*. **2012**, *24* (17), 3299–3306. DOI: 10.1021/cm203853f.

(34) Vasquez, V. R.; Williams, B. C.; Graeve, O. A. Stability and comparative analysis of AOT/water/isooctane reverse micelle system using dynamic light scattering and molecular dynamics. *J. Phys. Chem. B* **2011**, *115* (12), 2979–2987. DOI: 10.1021/jp109202f.

(35) Graeve, O. A.; Madadi, A.; Kanakala, R.; Sinha, K. Analysis of particle and crystallite size in tungsten nanopowder synthesis. *Metall. Mater. Trans. A* **2010**, *41* (10), 2691–2697. DOI: 10.1007/s11661-010-0280-9.

(36) Graeve, O. A.; Sinha, K. Dynamic light scattering study of reverse micellar systems for the synthesis of iron-based nanofluids. *Int. J. Mod. Phys. B* **2007**, *21* (28-29), 4774–4781. DOI: 10.1142/S0217979207045657.

(37) Vargas-Consuelos, C. I.; Seo, K.; Camacho-López, M.; Graeve, O. A. Correlation between particle size and Raman vibrations in WO_3 powders. *J. Phys. Chem. C* **2014**, *118* (18), 9531−9537. DOI: 10.1021/jp501095y.

(38) Zavala-Sanchez, L. A.; Hirata, G.; Novitskaya, E.; Karandikar, K.; Herrera, M.; Graeve, O. A. Distribution of Eu^{2+} and Eu^{3+} ions in hydroxyapatite: A cathodoluminescence and Raman study. *ACS Biomater. Sci. Eng*. **2015**, *1* (12), 1306−1313. DOI: 10.1021/acsbiomaterials.5b00378.

(39) Zavala, L. A.; Fernandez, P.; Novitskaya, E.; Diaz, J. N.; Herrera, M.; Graeve, O. A. Interconfigurational and intraconfigurational transitions of Yb^{2+} and Yb^{3+} ions in hydroxyapatite: A cathodoluminescence study. *Acta Mater*. **2017**, *135*, 35−43. DOI: 10.1016/j.actamat.2017.06.003.

(40) Stoll, S.; Schweiger, A. EasySpin, a comprehensive software package for spectral simulation and analysis in EPR. *J. Magn. Reson.* **2006**, *178* (1), 42−55. DOI: 10.1016/j.jmr.2005.08.013.

(41) Blöchl, P. E. Projector augmented-wave method. *Phys. Rev. B: Condens. Matter* **1994**, *50* (24), 17953−17979. DOI: 10.1103/PhysRevB.50.17953.

(42) Perdew, J. P.; Burke, K.; Ernzerhof, M. Generalized gradient approximation made simple. *Phys. Rev. Lett.* **1996**, *77* (18), 3865−3868. DOI: 10.1103/PhysRevLett.77.3865.

(43) Chagas da Silva, M.; Lorke, M.; Aradi, B.; Tabriz, M. F.; Frauenheim, T.; Rubio, A.; Rocca, D.; Deák, P. Self-consistent potential correction for charged periodic systems. *Phys. Rev. B: Condens. Matter* **2021**, *126* (7), 076401. DOI: 10.1103/PhysRevLett.126.076401.

(44) Wei, S. -H.; Zhang, S. B. Chemical trends of defect formation and doping limit in II-VI semiconductors: The case of CdTe. *Phys. Rev. B* **2002**, *66* (15), 155211. DOI: 10.1103/PhysRevB.66.155211.

(45) Novitskaya, E.; Kelly, J. P.; Bhaduri, S.; Graeve, O. A. A review of solution combustion synthesis: An analysis of parameters controlling powder characteristics. *Int. Mater. Rev.* **2021**, *66* (3), 188–214. DOI: 10.1080/09506608.2020.1765603.

(46) Dunbar, T. D.; Warren, W. L.; Tuttle, B. A.; Randall, C. A.; Tsur, Y. Electron paramagnetic resonance investigations of lanthanide-doped barium titanate: dopant site occupancy. *J. Chem. Phys. B* **2004**, *108* (3), 908–917. DOI: 10.1021/jp036542v.

(47) Kolodiazhnyi, T.; Petric, A. Analysis of point defects in polycrystalline $BaTiO_3$ by electron paramagnetic resonance. *J. Phys. Chem. Solids* **2003**, *64* (6), 953–960. DOI: 10.1016/S0022-3697(02)00454-7.

(48) Lu, D. -Y.; Liu, T. -T. Dielectric properties and defect chemistry of $(Ba_{1-x}La_x)(Ti_{1-x}Lu_x)O_3$ ceramics. *J. Alloys Compd.* **2017**, *698*, 967–976. DOI: 10.1016/j.jallcom.2016.12.272.

(49) Avinash, M.; Muralidharan, M.; Selvakumar, S.; Hussain, S.; Sivaji, K. Induced ferromagnetism and enhanced optical behaviour in indium-doped barium stannate system. *J. Mater. Sci.: Mater. Electron.* **2020**, *31* (1), 3375–3386. DOI: 10.1007/s10854-020-02886-x.

(50) Kutty, T. R. N.; Murugaraj, P.; Gajbhiye, N. S. Activation of trap centres in PTC $BaTiO_3$. *Mater. Lett.* **1984**, *2* (5), 396–400. DOI: 10.1016/0167-577X(84)90119-8.

(51) Zhang, C.; Yang, J.; Lin, C.; Li, C.; Lin, J. Reduction of Eu^{3+} to Eu^{2+} in $MAl_2Si_2O_8$ (M = Ca, Sr, Ba) in air condition. *J. Solid State Chem.* **2009**, *182* (7), 1673−1678. DOI: 10.1016/j.jssc.2009.04.009.

(52) Im, I. B.; Kim, Y.- I.; Jeon, D. Y. Thermal stability study of $BaAl_2Si_2O_8:Eu^{2+}$ phosphor using its polymorphism for plasma display panel application. *Chem. Mater.* **2006**, *18* (5), 1190−1195. DOI: 10.1021/cm051894v.

(53) Yacobi, B. G.; Holt, D. B. Cathodoluminescence scanning electron microscopy of semiconductors. *J. Appl. Phys.* **1986**, *59* (4), R1−R24. DOI: 10.1063/1.336491.

(54) Kociak, M.; Zagonel, L. F. Cathodoluminescence in the scanning transmission electron microscope. *Ultramicroscopy* **2017**, *176*, 112−131. DOI: 10.1016/j.ultramic.2017.03.014.

(55) Henderson, B. Spectroscopic effects of disorder in laser materials. *Contemp. Phys.* **2002**, *43* (2), 273−300. DOI: 10.1080/00107510110120812.

(56) Joy, D. C.; Luo, S. An empirical stopping power relationship for low-energy electrons. *Scanning* **1989**, *11* (4), 176−180. DOI: 10.1002/sca.4950110404.

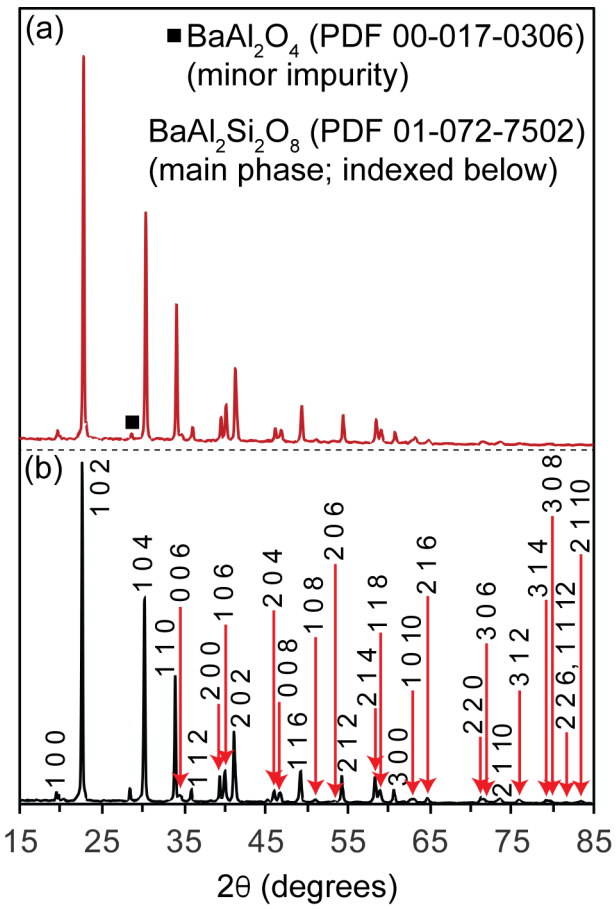

Figure 1. X-ray diffraction patterns of the (a) *h*–BAS and (b) *h*–BAS:Eu powders.

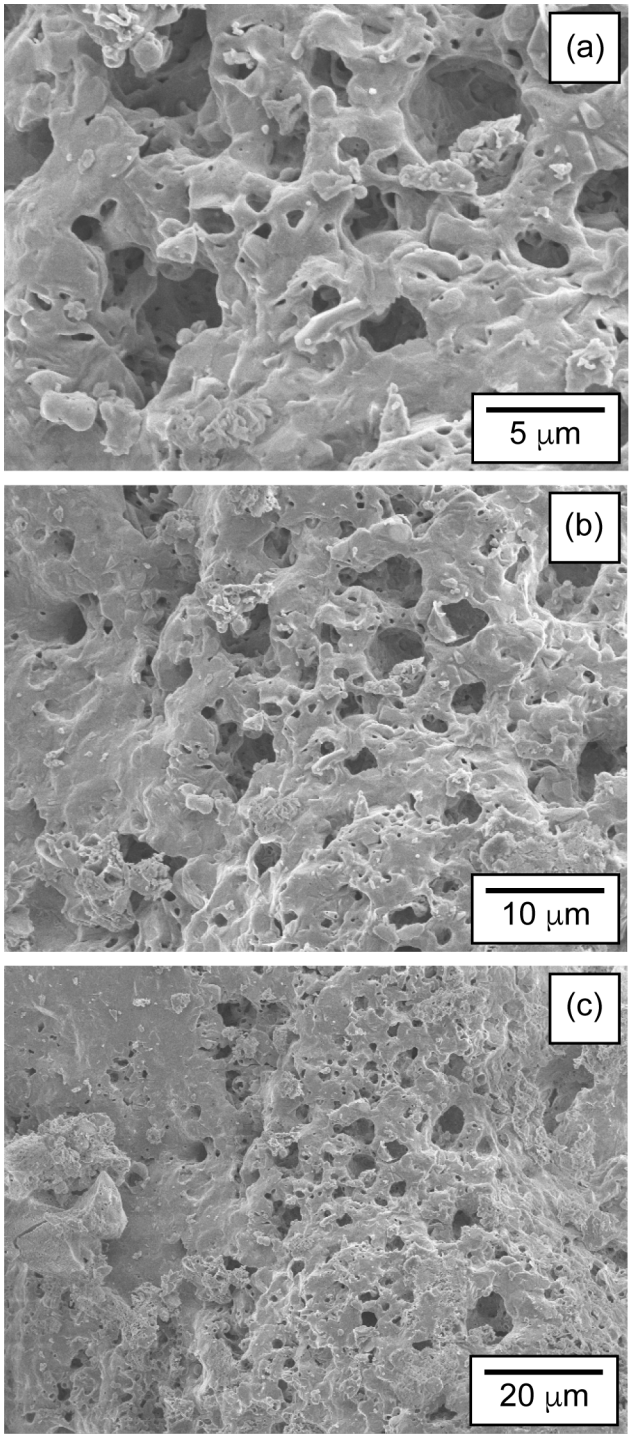

Figure 2. Scanning electron micrographs of the *h*–BAS:Eu powders.

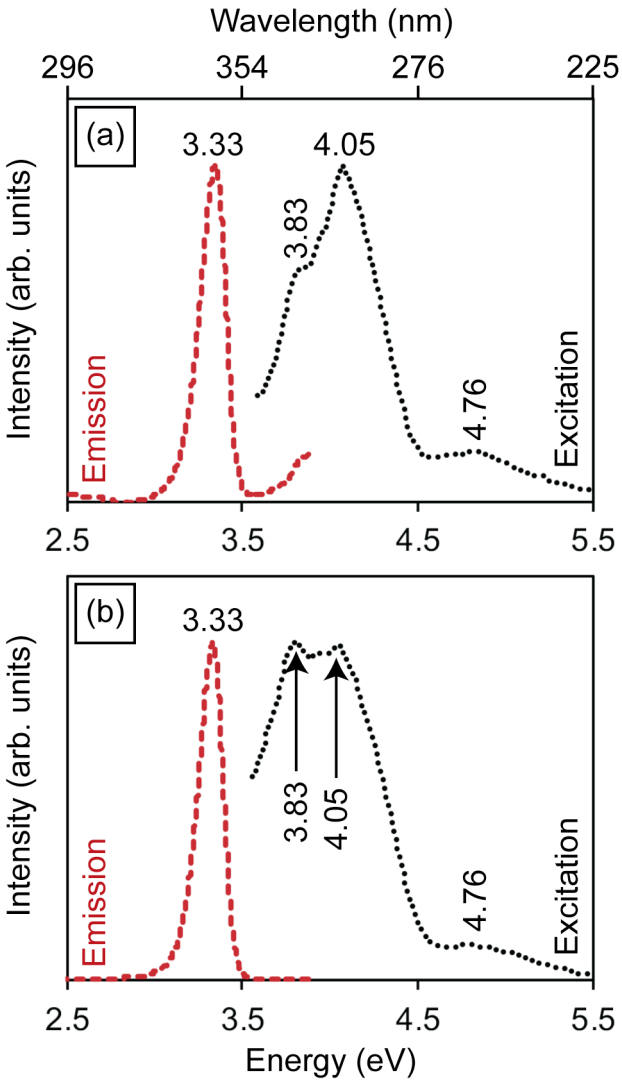

Figure 3. Excitation and emission spectra of the (a) *h*–BAS and (b) *h*–BAS:Eu powders obtained using a Xe lamp as excitation source.

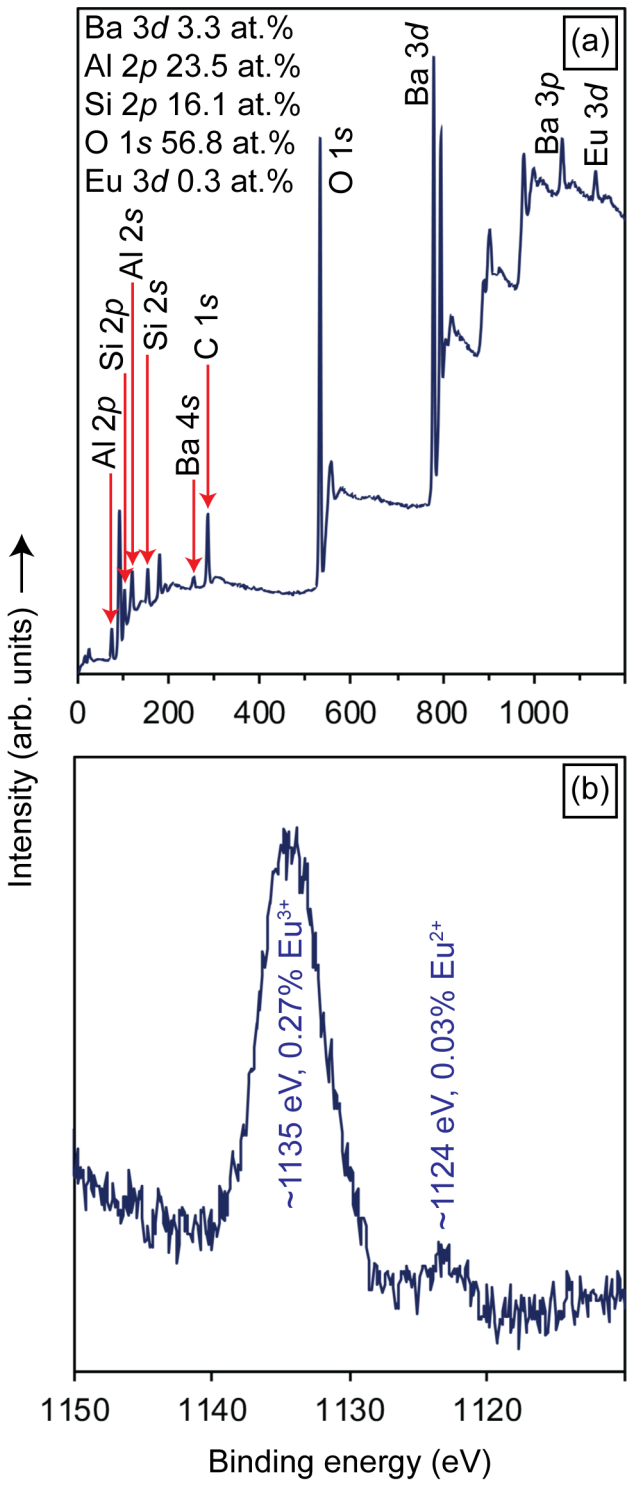

Figure 4. (a) Survey X-ray photoelectron spectra of the *h*–BAS:Eu powders and (b) the corresponding Eu $3d_{5/2}$ signal.

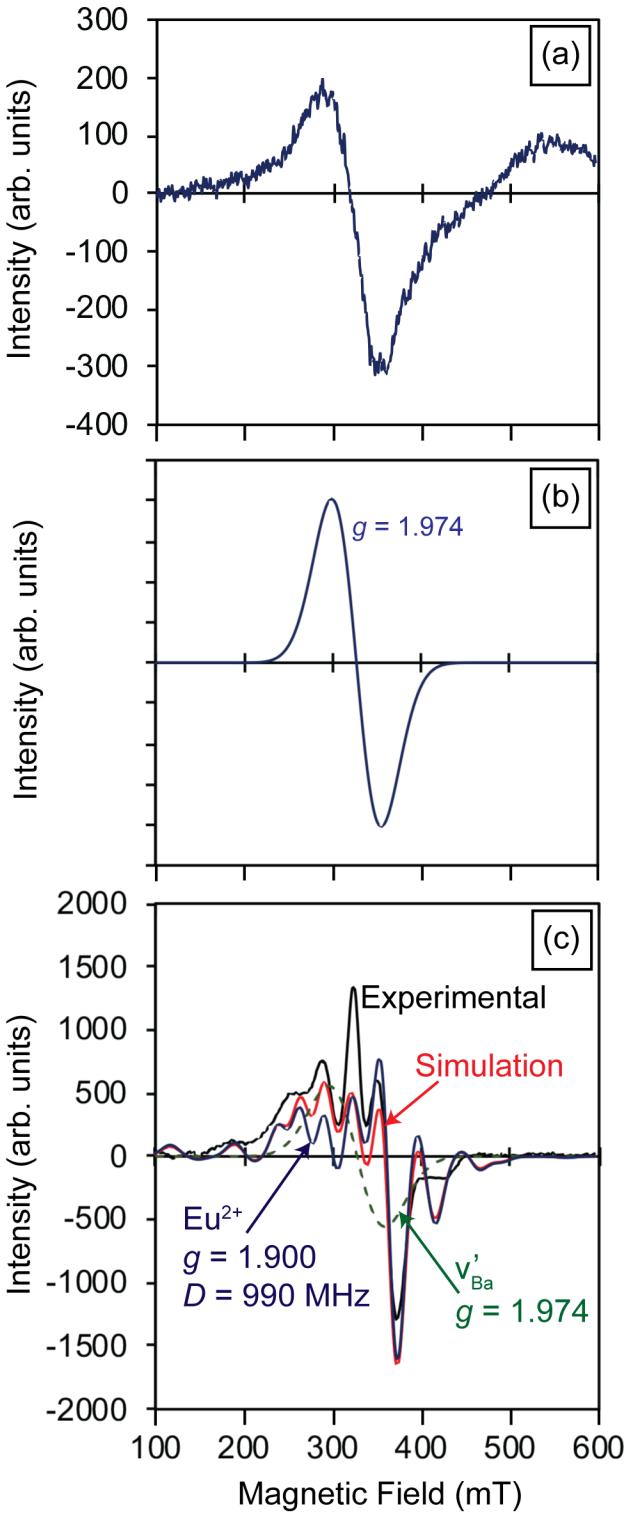

Figure 5. (a) Electron paramagnetic resonance (EPR) measurements for *h*-BAS and (b) simulated spectrum with a signal associated to singly-ionized barium vacancies (V'_{Ba}). (c) Experimental and simulated EPR spectra for the *h*-BAS:Eu powders. The simulated spectrum comprises the V'_{Ba} signal and the EPR multiplets generated by the interaction between the unpaired electrons in the 4*f* orbitals of Eu^{2+}, calculated with an axial zero-field splitting parameter of $D = 990$ MHz.

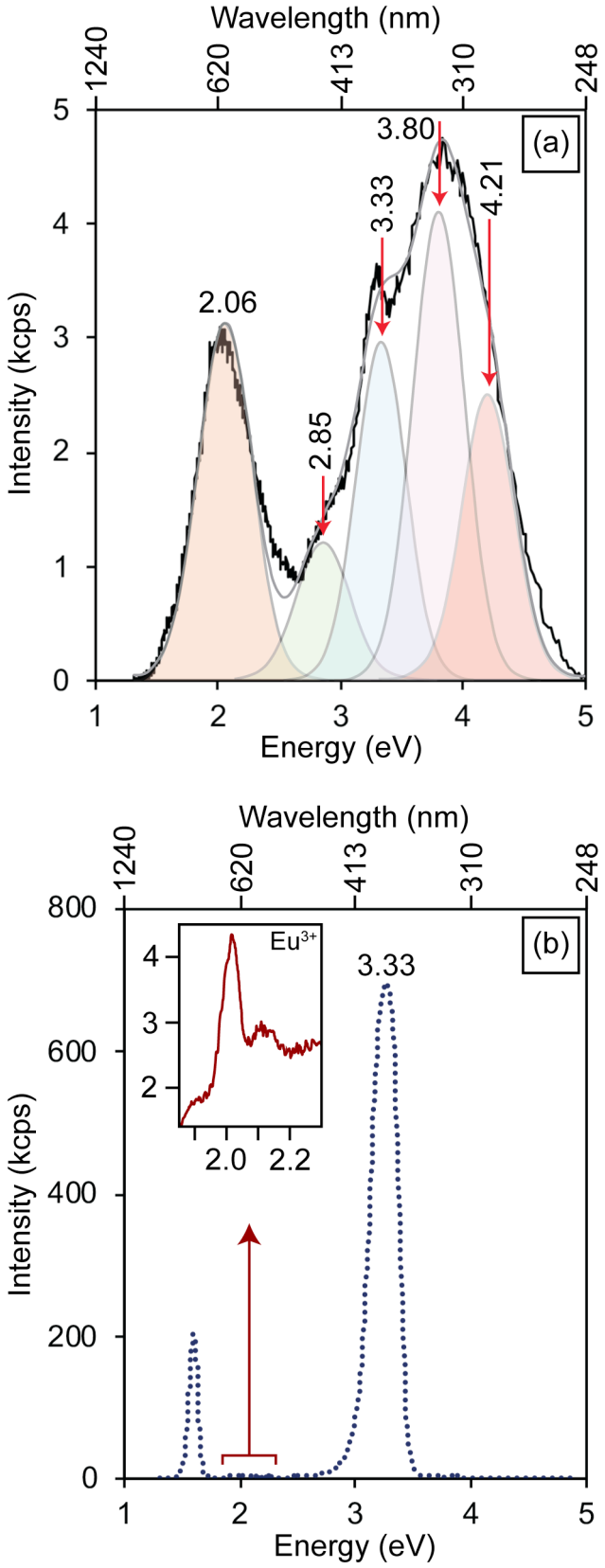

Figure 6. Cathodoluminescence spectra of the (a) *h*–BAS, and (b) *h*–BAS:Eu powders.

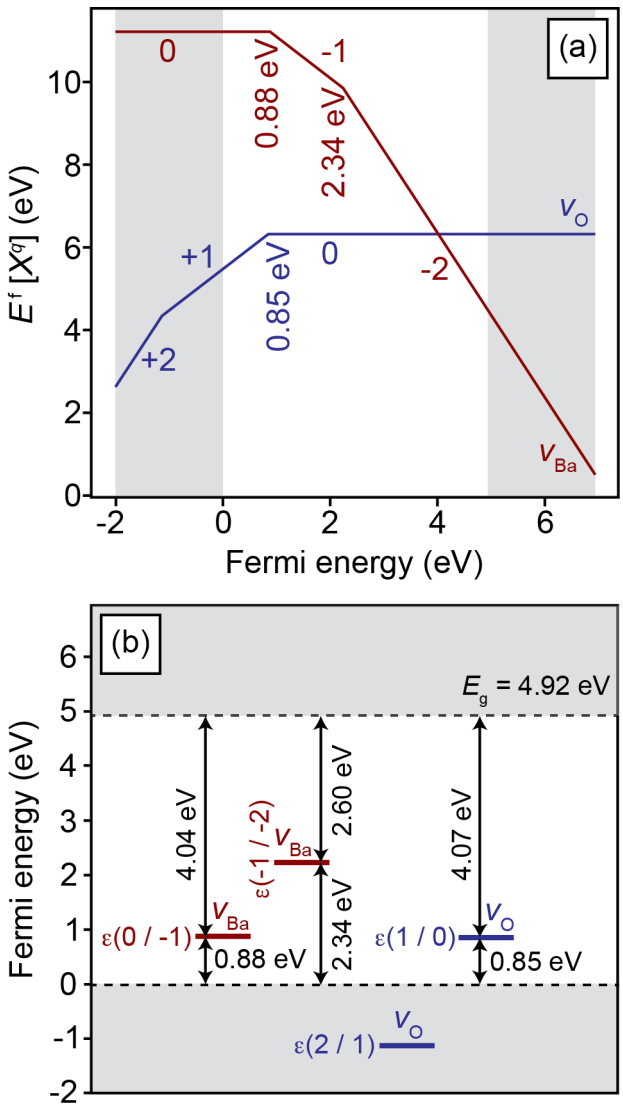

Figure 7. (a) The computed formation energy of a defect X of charge q ($E^f [X^q]$) with respect to the Fermi energy for barium vacancies and oxygen vacancies in *h*–BAS. (b) Thermodynamic transition levels for barium vacancies and oxygen vacancies in *h*–BAS, calculated using the PBE functional. The label ε(q/q') indicates the transition energy level as computed from equation (2). Below a given transition level, charge q is stable. Above the line defined by the transition level, charge q' is stable.

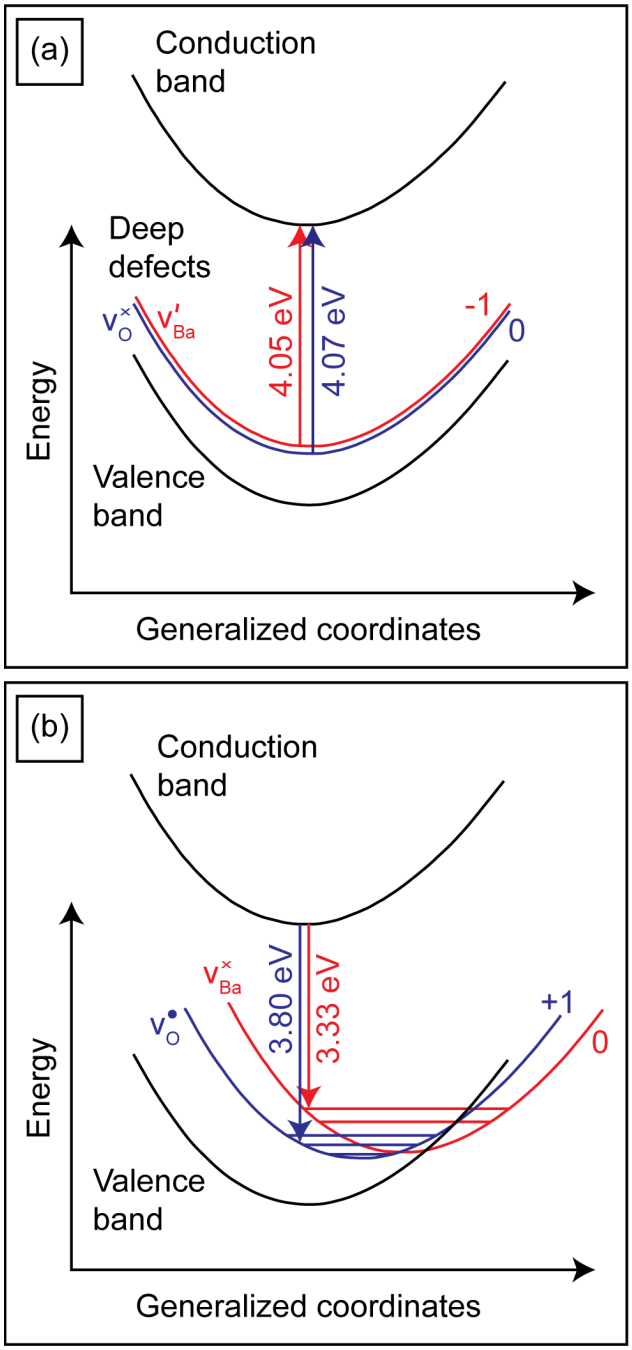

Figure 8. Schematic configuration coordinate diagram of oxygen and barium vacancy defects showing the (a) electronic excitation of the 4.05 eV band at zero-phonon line (ZPL) energy and the (b) electronic transitions corresponding to the 3.33 and 3.80 eV emissions with a Franck-Condon shift.

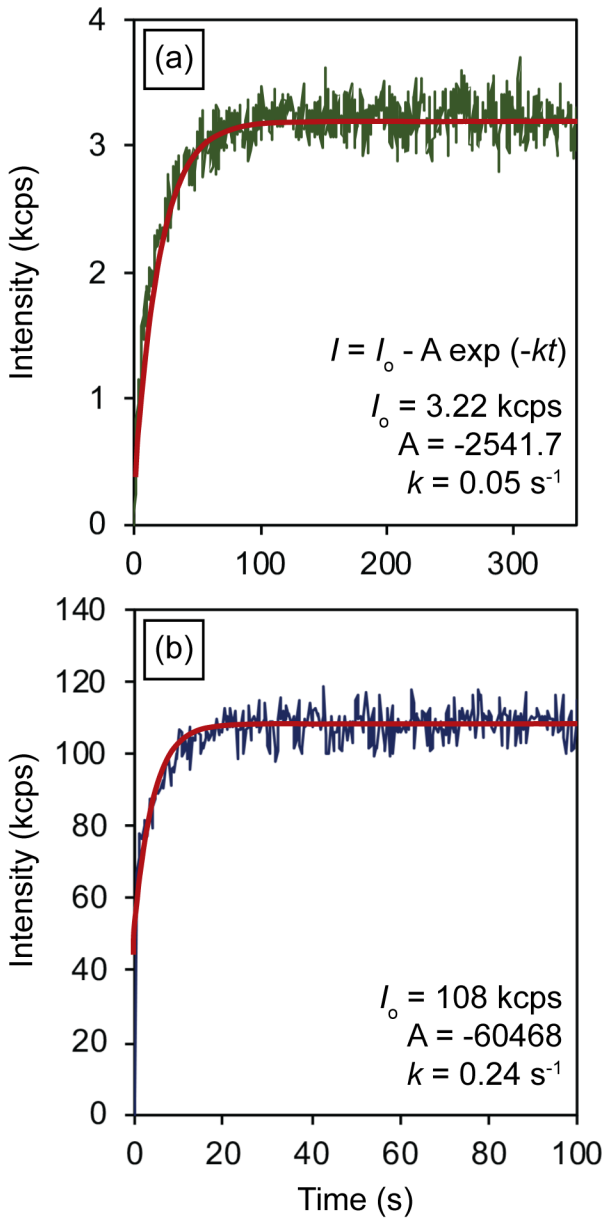

Figure 9. Curves of cathodoluminescence intensity of the 3.33 eV emission as a function of irradiation time for (a) *h*–BAS and (b) *h*–BAS:Eu fitted using an exponential equation.

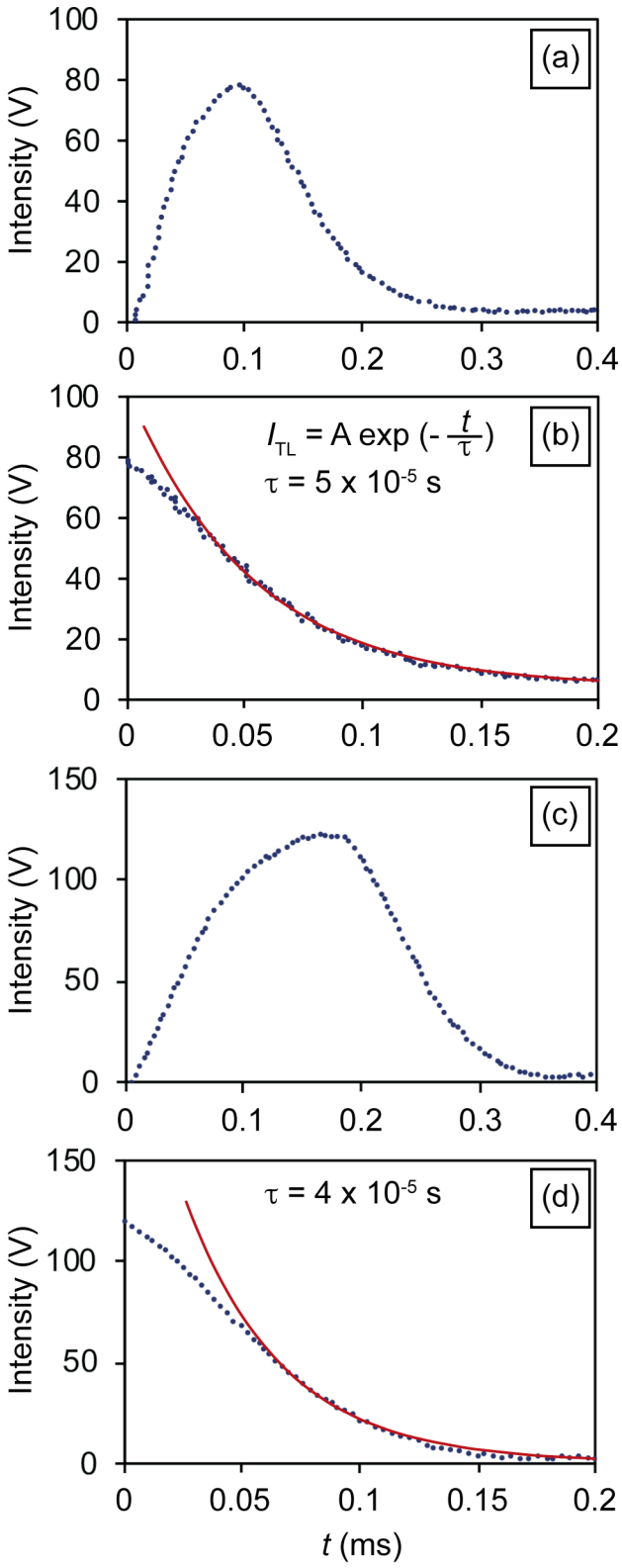

Figure 10. (a) Experimental triboluminescence spectrum and (b) corresponding simulated decay curve of the *h*–BAS powder; and (c) experimental triboluminescence spectrum and (d) corresponding simulated decay curve of the *h*–BAS:Eu powder.

Tables

Table 1. Absorbed energy per atom for different penetration depths of the electron beam on *h*–BAS calculated by Monte Carlo simulations.

Depth penetration of the electron beam (nm)	Percent of energy transferred (%)	Number of atoms irradiated per second (s^{-1})	Absorbed energy per atom (eV)
217.5	10	1.13×10^{12}	8.3
287.6	25	1.49×10^{12}	15.7
409.9	50	2.12×10^{12}	22.1
713.8	75	3.70×10^{12}	19.0
1107.5	90	5.73×10^{12}	14.7